Noble gas geochemistry of fluid inclusions in South African diamonds: implications for the origin of diamond-forming fluids

Suzette Timmerman[1], Masahiko Honda[1], David Phillips[2], Alan L. Jaques[1], Jeffrey W. Harris[3]

1.Research School of Earth Sciences, Australian National University, Acton, Australia

2.School of Earth Sciences, University of Melbourne, Parkville, Australia

3.School of Geographical and Earth Sciences, University of Glasgow, Glasgow, UK

Abstract

Fibrous diamond growth zones often contain abundant high-density fluid (HDF) inclusions and these provide the most direct information on diamond-forming fluids. Noble gases are incompatible elements and particularly useful in evaluating large-scale mantle processes. This study further constrains the evolution and origin of the HDFs by combining noble gas systematics with δ13C, N concentrations, and fluid inclusion compositions for 21 individual growth zones in 13 diamonds from the Finsch (n = 3), DeBeers Pool (n = 7), and Koffiefontein (n = 3) mines on the Kaapvaal Craton. C isotope compositions range from −2.8 to −8.6‰ and N contents vary between 268 and 867 at.ppm, except for one diamond with contents of <30 at.ppm N. Nine of the thirteen studied diamonds contained saline HDF inclusions, but the other four diamonds had carbonatitic or silicic HDF inclusions. Carbonatitic and silicic HDFs yielded low He concentrations, R/Ra ($^{3}He/^{4}He_{sample}/^{3}He/^{4}He_{air}$) values of 3.2–6.7, and low $^{40}Ar/^{36}Ar$ ratios of 390–1940. Noble gas characteristics of carbonatitic-silicic HDFs appear consistent with a subducted sediment origin and interaction with eclogite. Saline HDFs are characterised by high He concentrations, with R/Ra mostly between 3.9 and 5.7, and a wide range in $^{40}Ar/^{36}Ar$ ratios (389–30,200). The saline HDFs likely originated from subducted oceanic crust with low He but moderate Ar contents. Subsequent interaction of these saline HDFs with mantle peridotite could explain the increase in He concentrations and mantle-like He isotope composition, with the range in low to high $^{40}Ar/^{36}Ar$ ratios dependent on the initial ^{36}Ar content and extent of lithosphere interaction. The observed negative correlation between ^{4}He contents and R/Ra values in saline HDFs indicates significant in situ radiogenic ^{4}He production.

Keywords: Carbon, Fibrous diamond, High-density fluid (HDF), Noble gases, Subduction

Introduction

Sub-micrometer inclusions are found in fibrous diamonds, fibrous coats around octahedral diamonds, cloudy zones (Navon et al. 1988; Navon 1999), and along twin lines in monocrystalline diamonds (Jablon and Navon 2016). These sub-micrometer inclusions consist of minerals and/or HDFs. HDF inclusions probably reflect the diamond-forming medium and provide the most direct evidence on the source, composition and evolution of the diamond-forming fluids. It is important to constrain the origin and evolution of the diamond-forming media to better understand diamond formation and fluid evolution processes in the mantle.

Four end-member HDFs have been defined in diamonds, based on major element compositions: silicic, low-Mg carbonatitic, high-Mg carbonatitic, and saline HDFs (Schrauder and Navon 1994; Izraeli et al. 2001; Klein-BenDavid et al. 2009). Continuous arrays exist between the silicic and low-Mg carbonatitic end-member (e.g. Navon et al. 1988; Schrauder and Navon 1994), and between the saline and high-Mg carbonatitic end-member (Klein-BenDavid et al. 2004). Several studies have used these major element compositions to determine the processes that might explain the two arrays and evolution of the HDFs (Schrauder and Navon 1994; Klein-BenDavid et al. 2004, 2007; Weiss et al. 2015), such as fractional crystallisation, mixing, interaction with wall rock, and melt extraction. These studies have also provided important insights into the source(s) of these HDFs. However, the exact origin and evolution of the various HDF end-members remains poorly constrained. Trace elements of different HDF end-members have been determined in an attempt to further constrain HDF evolution. Trace element patterns without large anomalies ('planed'), and patterns with elevated Ba, U, Th, LREE and depleted Nb, Ta, and alkalis ('ribbed'), have been found in all HDF end-members (Weiss et al. 2013), showing that the trace elements are not directly coupled to the major elements. Based on $^{87}Sr/^{86}Sr$ compositions and trace element signatures, Weiss et al. (2015) suggested that the saline HDF was sourced from subducting slabs, and subsequently interacted with peridotitic lithospheric mantle to produce the carbonatitic HDFs; in contrast, interaction with eclogitic material might be responsible for silicic HDFs.

Noble gases are particularly sensitive indicators of mixing, melt migration, partial melting and degassing processes in the mantle, due to their extreme incompatibility and a wide range of high solubilities and diffusivities for the different noble gases. Thus, noble gases have the potential to provide new insights into the origin and evolution of diamond-bearing fluids. In addition, subducted material and sub-continental lithospheric mantle have very different noble gas elemental and isotopic compositions; therefore, noble gases can also be used to determine the influence of subducted components. To this end, we combine noble gas concentration and isotopic compositional data with HDF inclusion compositional information. As noble gases are primarily concentrated in the HDF inclusions in diamonds (Ozima and Zashu 1991; Johnson et al. 2000; Burgess et al. 2009), they provide an alternative approach to investigating the origin of diamond-forming fluids.

In this study, we present HDF major element compositions, He, Ar, and Xe isotope compositions and He-Ne-Ar-Kr-Xe elemental abundances for fibrous diamonds from the Finsch (n = 3), DeBeers Pool (n = 7) and Koffiefontein (n = 3) kimberlites. These kimberlites are located within the Archean Kaapvaal Craton and have yielded a vast array of xenoliths and diamonds for study. As a result, the geology of the underlying sub-continental lithospheric mantle (SCLM) is exceptionally well constrained, thus providing clear context for the interpretation of the new noble gas data. Consequently, the noble gas data provide new insights into the source(s) of diamond-forming fluids and the transfer of volatiles in the SCLM.

Geological background

The Finsch, DeBeers Pool and Koffiefontein kimberlites are located on the western margin of the Kimberley Block in the Kaapvaal Craton, South Africa. The Finsch kimberlite has an eruption age of ca.118 Ma (Smith et al. 1985) and is classified as an orangeite (or Group II kimberlite). The Koffiefontein (90.4 Ma; Davis 1978; Rickard et al. 1989) and DeBeers Pool kimberlites (84 Ma; Allsopp et al. 1989) have younger eruption ages and are classified as archetypal Group I kimberlites. Archaean monocrystalline peridotitic diamonds from DeBeers Pool were formed in a depleted dunite-harzburgitic mantle (Phillips et al. 2004), and over time the lithosphere beneath the Kimberley region was metasomatised, with more re-enriched lherzolite present in the mantle during Group I compared to Group II kimberlite events (Griffin et al. 2003). Based on counting statistics from inclusion-bearing diamonds (Gurney et al. 1979; Harris et al. 1984; Gurney et al. 1986; Wilding 1990; Rickard et al. 1989), all localities have diamonds with a dominantly peridotitic paragenesis that probably formed under lithospheric conditions. Previous studies have shown that fibrous diamonds from DeBeers Pool (Weiss et al. 2013) and Koffiefontein (Izraeli et al. 2001, 2004; Timmerman et al. 2018) commonly host saline HDFs, although a few carbonatitic and silicic HDF-bearing diamonds were also identified.

Analytical approach

Overview

Carbon isotope compositions, HDF inclusion compositions, N concentrations and aggregation states were measured in situ on core to rim transects, based on cathodoluminescence (CL) images of growth structures. Relevant CL images and photographs of the unpolished samples are shown in Electronic Supplementary Material 1. $\delta^{13}C_{VPDB}$ values were determined using the Sensitive High Resolution Ion Microprobe – Stable Isotopes (SHRIMP-SI), and N contents were obtained from Fourier-Transform infrared absorption (FTIR) analyses. HDF major element compositions were determined using energy-dispersive X-ray spectroscopy (EDS) in a scanning electron microscope (SEM; results in Electronic

Supplementary Material 2), and noble gas abundances and isotopic compositions were measured on a VG5400 mass spectrometer, using crushing experiments. Location identifiers preceding sample numbers are abbreviated to FIN (Finsch), DBP (DeBeers Pool), and KOF (Koffiefontein).

FTIR: nitrogen content

Each diamond was polished into thick plates along the 100 direction for cubic morphologies and 110 direction for dodecahedral shapes. The growth structure (see Electronic supplementary material 1) was recorded through CL imaging with a Robinson CL detector on a JEOL JSM-6610-A set at a beam of 15 kV. Spot measurements for nitrogen with a 100 × 100 μm aperture size along line transects were performed for diamonds FIN01, FIN03, KOF17, KOF18, KOF19 on a Hyperion2000 microscope attached to a Bruker FT-IR equipped with a KBr beam splitter, 15× condenser lens and liquid nitrogen cooled detector. Bulk spectra with a 1.2 mm aperture size were collected on the bench of the Bruker FT-IR for samples DBP7, DBP9, and DBP10. All spectra were taken in transmission mode from 4000 to 650 cm−1 for 200 scans at a resolution of 4 cm^{-1}. The opaqueness of fibrous diamonds results in difficulty in obtaining good transmission spectra. Diamonds FIN2, DBP6, DBP8, DBP14, and DBP15 were too opaque to collect any quantifiable infrared spectra. Further, the fit of the decomposition of spectra of diamond 3 was poor due to extremely low nitrogen concentrations. A background spectrum was taken before measuring each spectrum. After background and baseline corrections, normalisation to 1 cm thickness (11.94 cm^{-1}; Mendelssohn and Milledge 1995) and subtraction of a type II spectrum, each sample spectrum was decomposed into the different nitrogen components using the spreadsheet cabxd97n of D. Fisher (DTC research centre, UK). Replicate analyses indicate an internal error of ~10% in the estimation of nitrogen concentrations, total errors are higher, particularly for saturated spectra. The data of the spectra (without normalisation and substraction of type II spectrum) and images of the fit and residual after decomposing the spectrum in the nitrogen area are provided in Electronic Supplementary Material 3.

SHRIMP-SI: carbon isotope composition

Carbon isotope compositions were measured along core to rim traverses on the SHRIMP-SI with a 15 keV $^{133}Cs^{+}$ primary beam, 13 nA current and 27 μm spot size. Each analysis consisted of 6 backgrounds of 20 s and 6 sample scans of 20 s. Samples FIN01, FIN02, FIN03, KOF17, and KOF18 were measured on 6–7 July 2015 and yielded average standard values of −8.87 ± 0.27‰ (2sd) for MC08 (n = 57; −8.85‰ vs PDB; Stern et al. 2014) and − 24.87 ± 0.30‰ (2sd) for in-house standard BS249 (n = 61). Samples DBP06, DBP07, DBP08, DBP09, DBP10, DBP14, DBP15, and DBP19 were measured on 13–14 October 2015 and had standard values of −8.85 ± 0.31‰ (2sd) for MC08 (n = 27)

and −24.90 ± 0.19‰ (2sd) for in-house standard BS249 (n = 92). $\delta^{13}C$ values were calculated relative to PDB, based on the standard values of MC08. Typical signal counts were 2.8–2.9 × 109 cps for $^{12}C^-$ and 2.7–3.1 × 10^7 cps for $^{13}C^-$ on the 6–7 July and 3.4–3.9 × 10^9 cps for $^{12}C^-$ and 3.6–4.1 × 10^7 cps for $^{13}C^-$ on the 13–14 October 2015. The width of the source slit was 20 μm and the collector slit was 200 and 300 μm for ^{13}C and ^{12}C respectively.

SEM-EDS: major element composition and inclusion population density

Micro-inclusions were measured for the elements Na, K, Al, Si, Mg, Ca, Fe, Ti, P, Cl, and Ba and signals were collected with an 80 mm^2 X-max energy dispersive spectrometer on a Hitachi 4300 FE/SEM. Back scattered electron (BSE) imaging was used to find the inclusions, whereas secondary electron imaging was used to determine if the inclusion is below surface. The analyses were collected at 15 kV, a beam current of 1.3 nA and 60 s counting time and the data were reduced with a ZAF correction routine. The total of each analysis is dependent on the depth of the inclusion, its size and the amount of volatiles (carbonate, water). In order to compare the different analyses, the low total oxide (+Cl) contents were normalised to 100% on a carbon and water-free basis.

The BSE images were processed for colour intensity (black for diamond, lighter colours for inclusions) using the ImageJ software. Using the colour intensity counting statistics and assuming a back-scatter excitation depth of 1 μm, the percentage of micro-inclusions was estimated. The inclusion population density of each growth zone, estimated from BSE images, was compared to the inclusion population density estimated from the FTIR spectra. The peak height of each mineral in the FTIR spectra was converted to a ppm concentration (see Weiss et al. 2010) and all mineral concentrations were combined to estimate the total concentration of inclusions in the diamond samples (Electronic Supplementary Material 3). The above procedure was only relevant for the carbonatitic and silicic HDF-bearing diamonds (FIN01, FIN03, KOF17, KOF18), as halides in saline HDF-bearing diamonds are not detected by standard FTIR methods (Weiss et al. 2010); the latter problem results in an underestimation of inclusion population density. The results of the above two approaches are broadly similar (same order of magnitude), except for KOF17, which yielded large variations in FTIR peaks. This demonstrates that the BSE images can be used for a first order estimation of inclusion population densities (Electronic Supplementary Material 3).

Noble gas mass spectrometry

Diamond fragments were cleaned in conc. HF and 6 M HCl both at 110 °C overnight. Subsequently the fragments were placed in an ultrasonic bath for 10 min in Milli-Q water and finally distilled acetone before drying and weighing into stainless steel crusher vials. The crusher vials were cleaned by

scrubbing with sandpaper and demineralised water, followed by 15 min ultrasonic baths in acetone and 1:1 methanol: ethanol. After loading the samples, the crusher system was baked at 150 °C overnight and the sample system of the VG5400 noble gas mass spectrometer was baked for 14 h at 200 °C. Pre-crushing with 1000 strokes of an empty vial was performed to remove any air pockets from the system. Testing of a sample showed that with continued linear amounts of crushing the amount of gas release decreased exponentially. After 2000 strokes the diamond is powdered and starts to act as a buffer, preventing finer crushing. For this reason, blank and sample measurements consisted of 2000 strokes. The released gas was purified by a Ti bulk getter at 610 °C, trapped to a cold finger and let into the mass spectrometer with an acceleration voltage of 4.5 kV and trap current of 200 μA. All isotopes were measured with a Daly collector in analogue mode (feedback resistors on the Daly amplifier were 10^8, 10^7, 10^8, and 10^9 Ohm for Ne, Ar, Kr, and Xe respectively), except for ^{4}He and ^{40}Ar that were measured on a Faraday detector with a 10^{11} Ohm resistor. Total crushing blank levels were 2.76–19.8 × 10^{-10} ^{4}He, 2.53–8.20 × 10^{-14} ^{3}He, 4.17–9.57 × 10^{-12} ^{22}Ne, 1.07–17.2 × 10^{-8} ^{40}Ar, 6.08–150 × 10^{-14} ^{84}Kr, 8.09–5050 × 10^{-16} ^{132}Xe in ccSTP/g. All analyses were blank and neon interference corrected.

Results

N content and C isotope composition

Average N concentrations are generally in the range 300–800 at.ppm in the studied fibrous diamonds (Table 1), with individual spot determinations varying between 268 and 867 at.ppm (Table S3; Electronic Supplementary Material 2). One exception is ‘milky’ diamond FIN03, which contains very low N contents of <30 at.ppm. All the fibrous diamonds contain fully aggregated N pairs (Type IaA) and no platelet peaks were observed, except in KOF19. The C isotope compositions of the studied diamonds range from −2.8 to −8.6‰ (Table S4; Electronic Supplementary Material 2), extending the range typical of fibrous diamonds, which is −4 and − 8‰, (Boyd et al. 1992).

Micro-inclusion compositions

Most of the diamonds (9 of 13 diamonds) in this study have saline HDF inclusion compositions (Fig. 1a–d) and there were only one silicic, one low-Mg carbonatitic and two high-Mg carbonatitic HDF-bearing diamonds. Compared to saline HDF inclusions examined in previous studies (Izraeli et al. 2001, 2004; Tomlinson et al. 2006), the inclusions in this study are enriched in Na and slightly depleted in Si and Al (Fig. 1b). The carbonatitic to silicic HDF inclusions in this study have relatively higher Ca-Mg-Fe (Fig. 1b) compared to inclusions from other studies (Navon et al. 1988; Schrauder and Navon 1994). Diamond KOF19 likely contains a mixture of saline HDF/halide plus (K,Na)-carbonate inclusions, indicative of an association with a saline HDF composition.

Several diamonds contained micro-mineral inclusions (Table S1; Electronic Supplementary Material 2). Olivine with a Mg# (= 100 Mg/(Mg + Fe)) of 92.2–92.6 was found in diamonds DBP10 and DBP14; this composition is close to the mean for olivine inclusions from lherzolitic diamonds worldwide (Stachel and Harris 2008). Enstatite was present in diamonds DBP14 and DBP15 with Mg# ranging from 86 to 92.1, also within the known global range of 81.1–97.0 (Stachel and Harris 2008). The enstatite co-existing with olivine in diamond DBP14 has a Mg# of 92.1 and low Al2O3 contents (0.3 wt%), typical of peridotitic inclusions in diamonds (Stachel and Harris 2008), whereas enstatite inclusions in diamond DBP15 also have low CaO (<0.7 wt%), but a lower Mg# of 86 in the core and higher Al_2O_3 contents (3.2–7.2 wt%) similar to websteritic pyroxenes. An inclusion in the rim of DBP15 contains both pyroxene and apatite. The pyroxene has a composition similar to the pure enstatite in the same growth zone. Diamond KOF18 contained a peridotitic sulphide with >15 wt% Ni and 35 wt% S. Halides plus (K,Na)-carbonates with high K_2O/Na_2O were present in DBP07 (62 wt% K_2O) and KOF19 (65 wt% K_2O), and calcite was present in KOF17 (Table S1; Electronic Supplementary Material 2).

Sample separation based on chemical characteristics

The growth structures, C isotopic compositions, N contents, inclusion population densities and major element compositions were assessed to determine whether samples could be analysed as a single stone or required fragmentation into separate core, intermediate and rim zones for noble gas measurements. Samples were then broken according to differences in these characteristics to determine whether identifiable growth or compositional zones contain variable noble gas concentrations/compositions. Different growth zones were marked in different colours with permanent marker pens to identify them after breakage.

Based on large differences in inclusion population densities and growth structure (fibrous to polycrystalline), diamonds FIN01, DBP08, DBP09, and DBP15 were broken into separate growth zones. Most of the diamonds have consistent $\delta^{13}C_{VPDB}$ values throughout the diamond; exceptions include diamonds DBP07 (1.6‰ difference between core and rim) and DBP10 (3‰ difference between core and intermediate-rim zones; Table S4; Electronic Supplementary Material 2) and these growth zone fragments were used for separate noble gas analyses. Diamonds KOF17 and (possibly) KOF19 showed a decrease in nitrogen content towards the rim (Table S3; Electronic Supplementary Material 2), and were separated into two fractions (core and rim) for noble gas analyses.

Noble gas isotope compositions and abundances

^{4}He concentrations in the diamonds have a wide range from 0.3 to 65.1 × 10^{-6} ccSTP/g (Fig. 2a), which in part may be related to differences in inclusion population densities. Diamonds with saline HDF

inclusions generally exhibit higher He concentrations than diamonds with silicic and carbonatitic HDF inclusions (Fig. 2a). Diamonds from DeBeers Pool have higher ^{4}He concentrations (3.4–65.1 × 10^{-6} ccSTP/g) than those from Finsch (0.4–4.1 × 10^{-6} ccSTP/g) and Koffiefontein (0.3–2.5 × 10^{-6} ccSTP/g; Table 2). R/Ra values (where Ra is the atmospheric ^{3}He/^{4}He ratio of 1.42 × 10^{-6}) range from 1.9 to 6.7. A relatively large range in R/Ra (3.2–6.7) is found in silicic and carbonatitic HDF-bearing diamonds of this study, given their low ^{4}He concentrations (Fig. 2b). The saline diamonds show a decreasing R/Ra from 5.7 to 1.9 with increasing ^{4}He concentrations. Most of the R/Ra values fall within the known range for the sub-continental lithospheric mantle (average R/Ra of 5.9 ± 1.2; Day et al. 2005) and are similar to fibrous diamonds studied using noble gas step-heating methods (3.0–7.2 R/Ra for Panda, Canada; Jwaneng, Botswana; and the Congo; Burgess et al. 1998; Wada and Matsuda 1998; Burgess et al. 2009). Despite the large differences in He concentrations, the concentrations of the heavy noble gases for the different HDF end-members overlap (Fig. 2c; Table 2). The silicic and low-Mg carbonatitic diamonds have low ^{40}Ar/^{36}Ar ratios of 1236–1543; the high-Mg carbonatitic diamonds have ratios of 389–1942; and the saline diamonds have ^{40}Ar/^{36}Ar ratios of 382–30,200. The ^{40}Ar/^{36}Ar ratios are all higher than the atmospheric value (298.6; Lee et al. 2006), with a few saline samples having elevated ^{40}Ar/^{36}Ar ratios approaching MORB/SCLM values (Mid Oceanic Ridge Basalts; Sub-Continental Lithospheric Mantle) of >28,000 (Staudacher et al. 1989). Elemental fractionation of noble gases was investigated by referencing the concentration of the stable isotopes to ^{36}Ar, and subsequently normalizing to MORB values (Moreira et al. 1998). Most of the relative noble gas (^{3}He, ^{22}Ne, ^{36}Ar, ^{84}Kr, ^{130}Xe relative to ^{36}Ar) elemental abundance patterns are similar (Fig. 2e). The ^{3}He/^{36}Ar ratios of the samples are between that of MORB and OIB basalts (Moreira et al. 1998), whereas Ne-Kr/Ar values are similar to MORB, and ^{130}Xe/^{36}Ar ratios are relatively enriched, above MORB values (Fig. 2e). Most Kr isotopic compositions are within uncertainty (at 2SD) of air values, and some samples indicate possible isotopic mass fractionation generated by atmospheric Kr (Fig. 2d; Table S5; Electronic Supplementary Material 2); consequently, these results are not discussed further. Xe isotopic compositions observed in high-Mg carbonatitic and saline diamond samples lie on a mixing line between air and MORB (Staudacher and Allègre 1982) (Fig. 2f). Three samples (FIN02, DBP08a, DBP15b) lie on a mixing line between crustal and atmospheric Xe (Fig. 2f).

Discussion

Causes of differences in noble gas concentrations and isotopic compositions

The saline HDF-bearing diamonds from DeBeers Pool (this study) and from Panda on the Slave Craton (Burgess et al. 2009) are characterised by high He concentrations (18 of 21 measurements have >5.7 × 10^{-6} ccSTP/g) and a limited range in R/Ra (3.8–5.7 and one lower value of 1.9; Fig. 2b). Carbonatitic HDF-bearing diamonds from Finsch and Koffiefontein (this study) and a single carbonatitic HDF-

bearing diamond from Panda (Burgess et al. 2009) exhibit low R/Ra values (3.0–4.8) for their relatively low 4He concentrations (<2.5 × 10^{-6} ccSTP/g), compared to those observed in the measured saline growth zones (3 of 17) that exhibit similarly low ^{4}He concentrations, but higher R/Ra values (R/Ra of 5.0–5.7). As there is an apparent correlation between HDF compositions and He concentrations (Fig. 5a), but not with Ar-Kr-Xe concentrations, the differences in He concentration cannot be caused simply by differences in inclusion population densities and must be related to HDF composition. As each HDF type has its own characteristics, the abundance and isotopic compositional differences between the different HDF end-members are likely related to the source and evolution of the HDF(s). Influences on the He and Ar abundances and isotopic compositions by the radiogenic ingrowth of ^{4}He and ^{40}Ar, and fluid processes in the mantle and the original source region are discussed below.

In-situ radiogenic ^{4}He and ^{40}Ar ingrowth

After diamond formation, α-particles (^{4}He) in the HDF inclusions are generated from the decay of ^{238}U to ^{206}Pb, ^{235}U to ^{207}Pb, ^{232}Th to ^{208}Pb, and ^{147}Sm to ^{143}Nd. ^{40}Ar is formed by the decay of ^{40}K. In this study, the saline HDFs show a negative correlation between R/Ra and ^{4}He concentrations (Fig. 2b), suggesting the addition of in situ produced radiogenic ^{4}He over time. In addition, the ^{40}Ar/^{36}Ar ratios are generally higher for HDFs rich in K (saline) than in HDFs poor in K (silicic, carbonatitic), indicating addition of in situ produced radiogenic ^{40}Ar. Furthermore, a correlation exists between ^{4}He and ^{40}Ar. This suggests that both radiogenic ^{4}He and ^{40}Ar ingrowth may be significant. For example, the importance of ^{4}He ingrowth becomes clear in diamonds DBP09 and DBP15, where growth zones were divided on the basis of differences in inclusion population density. For both diamonds the core has much higher He concentrations, with lower R/Ra values, compared to the intermediate and rim zones (e.g. Fig. 3). This might be caused by higher U-Th/^{3}He ratios in the core and/or a longer time period for ingrowth of radiogenic ^{4}He. The preserved differences in isotopic compositions and concentrations between growth zones in diamonds DBP09 and DBP15 also confirm the slow rates of He diffusion reported in prior studies of natural diamonds (see also Kurz et al. 1987), and indicate that He from HDF inclusions is unlikely to re-distribute uniformly within a diamond after its formation. No significant differences in He isotope compositions were found in diamonds where growth zones were separated based on N, δ^{13}C, or growth structure.

Literature data (Schrauder et al. 1996; Weiss et al. 2013) show that silicic diamonds have a larger spread in U/K ratios and U concentrations than saline diamonds. These data can be used to calculate the minimum and maximum ingrowth amounts of ^{40}Ar and ^{4}He (see Fig. 4 caption for equations). If we consider ingrowth of ^{40}Ar after kimberlite eruption, and assume a minimum ^{40}Ar/^{36}Ar ratio of 381, based on the lowest measured ratios in our samples (Fig. 4a), then the higher K contents in the saline HDF

inclusions can explain most, but not all, the variation in $^{40}Ar/^{36}Ar$ values. This conclusion is, of course, predicated on the assumption that all ^{40}Ar and ^{36}Ar was extracted from HDF inclusions. If some proportion of the argon remained trapped in unexposed HDF inclusions in the diamond, then the modelled maximum ^{40}Ar ingrowth amount is an upper estimate. For He isotope compositions, the majority of results for saline diamonds can be explained by ^{4}He ingrowth after kimberlite eruption, assuming a starting composition 7.7 R/Ra, thus accounting for even the highest R/Ra values (Fig. 4b). Further studies are needed to determine both U-Th-K and noble gas data on the same diamonds. Some fibrous diamonds could be significantly older than the host kimberlite eruption age, as indicated by the presence of nitrogen in B-centres (Type IaAB) in some fibrous diamonds from Finsch and DeBeers Pool, South Africa (e.g. Weiss et al. 2014; Weiss et al. 2018) and Russia (e.g. Zedgenizov et al. 2006). However, as discussed below, the variations noted above could also be caused by fluid processes in the mantle and the source region.

Fluid and mantle processes

General remarks

Given the differences in the range of He and Ar elemental and isotopic compositions between saline, silicic and carbonatitic HDFs, radiogenic ingrowth cannot be the only factor responsible for variations in the observed present-day noble gas compositions. Fractional crystallisation, immiscibility, mixing, and interaction with the wall-rock have been suggested as possible causes for the continuous major element arrays observed between saline and high-Mg carbonatitic and between silicic and low-Mg carbonatitic HDFs (Klein-BenDavid et al. 2007 and references therein). These possibilities are discussed below in the light of the noble gas data.

Fractional crystallisation

The changes in major element composition from carbonatitic to silicic HDF have been attributed to fractional crystallisation of carbonates and other phases (Schrauder and Navon 1994). However, fractional crystallisation of minerals is highly unlikely to cause differences in noble gas isotope compositions, as all noble gases are highly incompatible; for example, ^{40}Ar will not fractionate from ^{36}Ar at mantle temperatures. Therefore, the comparable He and Ar isotope compositions in carbonatitic and silicic HDFs indicate fractional crystallisation is a possible mechanism to explain the evolution from carbonatitic to silicic compositions. However, given the difference in $^{40}Ar/^{36}Ar$ ratios between high-Mg carbonatitic (390–680) and saline HDFs (380–30,200), HDF evolution from carbonatitic to saline compositions, or vice versa, cannot be explained by fractional crystallisation processes.

Immiscibility

The compositional gap between silicic and saline HDF inclusions has been attributed to separation of an immiscible carbonatitic fluid after the crystallisation of Mg-carbonates (Klein-BenDavid et al. 2007). Lighter noble gases diffuse faster than heavier noble gases (Burnard 2004) and could partition preferentially into the fluid. In addition to elemental fractionation of Ar-Kr-Xe with respect to He, fractionation of K from U-Th, and high field strength elements from noble gases are also possible (during immiscibility). At present the extent of this fractionation is not known, but low pressure (1 GPa), medium temperature (800 °C) experiments of immiscible chloride-silicate melts indicate that K partitions preferentially into the chloride melt, whereas U and Th partition into the silicate melt (Veksler et al. 2012). Similar processes should result in systematic differences in $^{40}Ar/^{36}Ar$ and $^{4}He/^{3}He$ ratios over time between the silicic and saline HDFs. Although fundamental data, including partitioning of noble gases are not available, several features appear inconsistent with HDF evolution by immiscibility. These include the generally higher U concentrations (Weiss et al. 2013; Schrauder et al. 1996) but higher R/Ra values for a given ^{3}He concentration in diamonds with saline HDFs compared to those with silicic to low Mg carbonatitic HDFs. In addition, although He concentrations are higher in diamonds with saline HDFs, concentrations of heavy noble gases appear to be similar in both silicic-carbonatititic and saline diamonds.

Mixing

Trace elements and Sr-Nd-Pb isotopic compositions of fibrous diamonds have been used as evidence for mixed fluids (Klein-BenDavid et al. 2010). Some of the variation in noble gas compositions could potentially be caused by mixing between different HDFs. Helium (both ^{3}He and ^{4}He) concentrations generally decrease with increasing MgO (Fig. 5a), SiO_2, Al_2O_3, and CaO of the HDF (Fig. 5; only HDF compositions were used and no mineral compositions). The $^{40}Ar/^{36}Ar$ ratios are commonly lower with increasing MgO content and decreasing Cl content (Fig. 5b, c). However, these trends do not follow a perfect mixing line, implying that mixing is not the only process involved.

Interaction with the wall-rock

Metasomatic interaction of HDFs with the wall rock in the SCLM, either eclogitic or peridotitic, has been suggested as a process capable of generating variations from carbonatitic to silicic or saline HDFs (Klein-BenDavid et al. 2007). A decrease in Mg# found from carbonatitic to silicic or saline compositions could be evidence of interaction with the wall rock (Klein-BenDavid et al. 2007).

Interaction with peridotite will result in a shift in noble gas compositions towards higher $^{40}Ar/^{36}Ar$ ratios (up to 40,000; assuming the SCLM has $^{40}Ar/^{36}Ar$ ratios similar to those observed in MORBs based on $^{40}Ar/^{36}Ar$ ratios measured in diamonds from the SCLM; Burgess et al. 2009) and R/Ra values of 5.9 ± 1.2 (Day et al. 2005). Some of the saline HDFs have elevated $^{40}Ar/^{36}Ar$ ratios (this study, Burgess et al. 2009) and R/Ra values of mostly 3.9–5.7, similar to peridotite in the SCLM. This suggests that the saline HDF noble gas characteristics could be explained by the influence of mantle peridotite. In addition, interaction with the wall-rock might account for the high He concentrations found in saline HDFs, because, during percolation through the SCLM prior to diamond formation, HDFs will scavenge light noble gases (Heber et al. 2007 and references therein). Fluid-rock interaction is a viable process to rapidly elevate He contents based on comparable ^4He concentrations in our HDFs ($\sim10^{-5}$ to 10^{-3} cm^3/g ^4He; corrected for inclusion population density) to calculated ^4He concentrations in HDFs (10^{-6} to 10^{-3} cm3/g) using melt-bulk rock partition coefficients (KdHe of $\sim10^{-4}$ to 6×10^{-3} in harzburgite; Parman et al. 2005; Jackson et al. 2013) and ^4He concentrations observed in lithospheric peridotite (10^{-9} to 10^{-6} cm^3/g ^4He; Day et al. 2005). The trend from saline to carbonatitic HDF compositions has been attributed to interaction with peridotitic wall rock (Weiss et al. 2015). In the present study, however, a trend towards more peridotitic noble gas characteristics is observed from high-Mg carbonatitic to saline HDFs (Fig. 5b, c with $^{40}Ar/^{36}Ar$ vs Cl and MgO content), which is the opposite to that predicted.

Conversely, silicic HDFs have been widely proposed to be related to eclogitic rocks (Weiss et al. 2015 and references therein). Assuming a subduction origin for the eclogite, these rocks should contain lower light noble gas concentrations compared to peridotitic rocks, due to He-Ne loss during subduction, making the residual component more susceptible to ingrowth of ^4He by U and Th supplied from the subducted material. This is consistent with the current limited data for silicic to low-Mg carbonatitic HDFs, which exhibit low ^3He concentrations, relatively low ^4He concentrations, but a range in R/Ra values consistent with at least some ^4He ingrowth. Fluids produced from water-rich sediments (MAG-1 USGS marine mud) during experiments at 5–7 GPa have similar major element compositions to silicic HDFs found in diamonds (Rapp et al. 2017) and support a subducted sediment origin for silicic diamond-forming fluids.

Origin of fluids

Previous studies have suggested kimberlitic fluids as the source of carbonatitic HDF-bearing diamonds (Boyd et al. 1992; Klein-BenDavid et al. 2007) and subducting slab fluids as the source for saline HDF-bearing diamonds (Weiss et al. 2015). Carbonatite rocks from Brazil, Russia and Tanzania are characterised by R/Ra values of 0.007 to 7.6 and $^{40}Ar/^{36}Ar$ ratios generally <5000 and as low as 302 (Tolstikhin et al. 1985; Javoy et al. 1989; Sasada et al. 1997). Olivine grains in kimberlites from Udachnaya-East show a smaller range of 1.2–5.5 R/Ra and low $^{40}Ar/^{36}Ar$ ratios of 1844–9150 (Sumino

et al. 2006), but may reflect mantle peridotite rather than the kimberlite magma as olivine grains can be xenocrystic. The low $^{40}Ar/^{36}Ar$ ratios and range in R/Ra reported for carbonatitic HDF-bearing diamonds in this study are consistent with the noble gas characteristics of kimberlites and carbonatites; therefore these potential sources cannot be excluded.

Some saline HDF inclusions in diamonds have similar noble gas signatures to peridotite from the sub-continental lithospheric mantle, with R/Ra values up to 5.7 and high $^{40}Ar/^{36}Ar$ ratios, likely through wall-rock interaction. Low $^{40}Ar/^{36}Ar$ ratios are likely caused by the involvement of a recycled component as $^{36}Ar/^{130}Xe$ and $^{84}Kr/^{130}Xe$ elemental ratios of all the measured fibrous diamonds in this study fall in the compositional field for sea-water, sediments and crustal end-members and are distinct from atmospheric Ar/Xe and Kr/Xe compositions (Fig. 5d). Xenon isotope compositions plot on air-MORB and air-crust (enriched in spontaneous fission Xe from ^{238}U) arrays, also indicative of mantle and crustal components (Fig. 2f). Various studies show heavy noble gases are subducted to some extent (Staudacher and Allègre 1988; Holland and Ballentine 2006; Kendrick et al. 2011). The low atmospheric abundance of He and Ne, low water solubility, high diffusivity of He in sedimentary material (Hilton et al. 1992) and the interaction of magmas with the crust during ascent and possible ^{4}He ingrowth (Hilton et al. 2002) have led to the conclusion that the light noble gases He and Ne are not significantly subducted into the mantle (Ballentine and Holland 2008). However, low R/Ra values can still be generated by low initial ^{3}He concentrations and radiogenic ^{4}He ingrowth in a few million years from high U and Th concentrations in slab-derived fluids (Brandon et al. 1999). A subducted sediment origin is consistent with the low He contents, range in R/Ra values, and low $^{40}Ar/^{36}Ar$ ratios of silicic to low-Mg carbonatitic diamonds. This interpretation is in keeping with the observation of similar I/Cl ratios in silicic African diamonds and marine sediments (see Fig. 5b of Burgess et al. 2009 and references therein). The low $^{40}Ar/^{36}Ar$ ratios of some saline diamonds are compatible with a subduction origin. Fluids released from the slab interacting with peridotite in the SCLM would rapidly elevate helium concentrations and produce a SCLM-like R/Ra value. As some argon is transported into the mantle by subduction, $^{40}Ar/^{36}Ar$ ratios are changed less easily upon interaction with peridotite in the SCLM. An origin for saline HDFs from the subducting slab is supported by relatively high Cl contents and Cl/K found in oceanic intraplate basalts, with Cl inferred to be sourced from recycled altered oceanic lithosphere (Stroncik and Haase 2004). A correlation between $^{40}Ar/^{36}Ar$ and $Cl/^{36}Ar$ ratios and between K and Cl is observed in African, Canadian, and Russian diamonds, with $^{40}Ar^*/Cl$ ratios similar to the upper mantle (Turner et al. 1990; Johnson et al. 2000; Burgess et al. 2002). These characteristics do not support a subduction origin and imply a relatively constant $^{40}Ar^*/Cl$ ratio for the HDFs and limited radiogenic ^{40}Ar ingrowth.

Conclusions

This research has resulted in two major conclusions. First, noble gas analyses of individual growth zones from 13 diamonds of the Finsch (n = 3), DeBeers Pool (n = 7), and Koffiefontein (n = 3) kimberlite mines reveal saline HDFs with high He concentrations, R/Ra values mostly between 3.9 and 5.7, and a wide range in $^{40}Ar/^{36}Ar$ ratios (389–30,200). Low-Mg carbonatitic, high-Mg carbonatitic and silicic HDFs are characterised by low He concentrations, R/Ra values of 3.2–6.7, and low $^{40}Ar/^{36}Ar$ ratios (<1940). The low Ar/Xe and Kr/Xe ratios are attributed to a sediment, crust and sea-water origin (subducted material). Low $^{40}Ar/^{36}Ar$ ratios of carbonatitic, silicic, and some saline HDFs also point to a subduction origin. These noble gas data are in agreement with a subducted sediment origin for silicic HDFs and a subducted oceanic crust origin for saline HDFs, based on major element, trace element and Sr isotope evidence of previous studies. Second, the radiogenic noble gas isotope (^{4}He and ^{40}Ar) compositions provide a time-integrated history of the fluid. The noble gases of some saline HDFs have R/Ra values and $^{40}Ar/^{36}Ar$ ratios similar to the SCLM, suggesting interaction with peridotitic wall-rock. A negative correlation between R/Ra and ^{4}He concentrations in saline diamonds is interpreted to result from in situ produced radiogenic ^{4}He ingrowth after diamond formation.

Acknowledgements

We thank Peter Holden (SHRIMP) and Xiaodong Zhang (VG5400) for their assistance with the analytical work. The authors acknowledge the facilities, and the scientific and technical assistance, of the Australian Microscopy and Microanalysis Research Facility at the Centre of Advanced Microscopy, The Australian National University. The Diamond Trading Company (a member of the DeBeers Group of Companies) is thanked for the donation of the diamonds used in this study to JWH. We thank Ray Burgess, Yaakov Weiss and editor Oded Navon for their helpful comments that greatly improved the presentation of this paper. This work was funded by the Australian Research Council (DP140101976) to MH, ALJ, DP, and Deborah Araujo, and AGRTP and Ringwood scholarships to ST.

References

Allsopp H, Bristow J, Smith C, Brown R, Gleadow A, Kramers J, Garvie O (1989) A summary of radiometric dating methods applicable to kimberlites and related rocks. In: Ross J et al (eds) Kimberlites and related rocks: Their composition, occurrence, origin and emplacement. Geol Soc Australia Spec Publ 14, vol 1. Blackwells Scientific Press, Oxford, pp 343–357

Ballentine CJ, Holland G (2008) What CO well gases tell us about the origin of noble gases in the mantle and their relationship to the atmosphere. Philos T Roy Soc A 366:4183–4203

Boyd S, Pillinger C, Milledge H, Mendelssohn M, Seal M (1992) C and N isotopic composition and the infrared absorption spectra of coated diamonds: evidence for the regional uniformity of CO2–H2O-rich fluids in lithospheric mantle. Earth Planet Sc Lett 109:633–644

Brandon AD, Becker H, Carlson RW, Shirey SB (1999) Isotopic constraints on time scales and mechanisms of slab material transport in the mantle wedge: evidence from the Simcoe mantle xenoliths, Washington, USA. Chem Geol 160:387–407

Burgess R, Cartigny P, Harrison D, Hobson E, Harris J (2009) Volatile composition of microinclusions in diamonds from the Panda kimberlite, Canada: Implications for chemical and isotopic heterogeneity in the mantle. Geochim Cosmochim Ac 73:1779–1794

Burgess R, Johnson L, Mattey D, Harris J, Turner G (1998) He, Ar and C isotopes in coated and polycrystalline diamonds. Chem Geol 146:205–217

Burgess R, Layzelle E, Turner G, Harris JW (2002) Constraints on the age and halogen composition of mantle fluids in Siberian coated diamonds. Earth Planet Sc Lett 197:193–203

Burnard P (2004) Diffusive fractionation of noble gases and helium isotopes during mantle melting. Earth Planet Sc Lett 220:287–295

Davis GL (1978) Zircons from the mantle. Carnegie I Wash 77:895–897

Day JM, Hilton DR, Pearson DG, Macpherson CG, Kjarsgaard BA, Janney PE (2005) Absence of a high time-integrated 3He/(U+ Th) source in the mantle beneath continents. Geology 33:733–736

Griffin WL, O'Reilly SY, Abe N, Aulbach S, Davies RM, Pearson NJ, Doyle BJ, Kivi K (2003) The origin and evolution of Archean lithospheric mantle. Precambrian Res 127:19–41

Gurney JJ, Harris JW, Rickard RS (1979) Silicate and oxide inclusions in diamonds from the Finsch kimberlite pipe. In: Boyd FR, Meyer HOA (eds) Kimberlites, diatremes, and diamonds: Their geology, petrology, and geochemistry. Am Geophys Union, pp 1–15

Gurney J, Harris J, Rickard R, Cardoso P (1986) Mineral inclusions in diamonds from Koffiefontein mine. Extended Abstracts, the Fourth Int Kimberlite Conference, pp 389−391

Harris J, Hawthorne J, Oosterveld M (1984) A comparison of diamond characteristics from the DeBeers pool mines, Kimberley, South Africa. Ann Sci Univ Clermont-Ferrand 74:1–13

Heber VS, Brooker RA, Kelley SP, Wood BJ (2007) Crystal–melt partitioning of noble gases (helium, neon, argon, krypton, and xenon) for olivine and clinopyroxene. Geochim Cosmochim Ac 71:1041–1061

Hilton D, Hoogewerff J, Van Bergen M, Hammerschmidt K (1992) Mapping magma sources in the east Sunda-Banda arcs, Indonesia: constraints from helium isotopes. Geochim Cosmochim Ac 56:851–859

Hilton DR, Fischer TP, Marty B (2002) Noble gases and volatile recycling at subduction zones. Rev Mineral Geochem 47:319–370

Holland G, Ballentine CJ (2006) Seawater subduction controls the heavy noble gas composition of the mantle. Nature 441:186–191

Izraeli ES, Harris JW, Navon O (2001) Brine inclusions in diamonds: a new upper mantle fluid. Earth Planet Sc Lett 187:323–332

Izraeli ES, Harri JW, Navon O (2004) Fluid and mineral inclusions in cloudy diamonds from Koffiefontein, South Africa. Geochim Cosmochim Ac 68:2561–2575

Jablon BM, Navon O (2016) Most diamonds were created equal. Earth Planet Sc Lett 443:41–47

Jackson CR, Parman SW, Kelley SP, Cooper RF (2013) Constraints on light noble gas partitioning at the conditions of spinel-peridotite melting. Earth Planet Sc Lett 384:178–187

Javoy M, Pineau F, Staudacher T, Cheminee J, Krafft M (1989) Mantle volatiles sampled from a continental rift: the 1988 eruption of Oldoinyo Lengai (Tanzania), Terra 1, p 324

Johnson L, Burgess R, Turner G, Milledge H, Harris J (2000) Noble gas and halogen geochemistry of mantle fluids: comparison of African and Canadian diamonds. Geochim Cosmochim Ac 64:717–732

Kendrick MA, Scambelluri M, Honda M, Phillips D (2011) High abundances of noble gas and chlorine delivered to the mantle by serpentinite subduction. Nat Geosci 4:807–812

Klein-BenDavid O, Izraeli ES, Hauri E, Navon O (2004) Mantle fluid evolution—a tale of one diamond. Lithos 77:243–253

Klein-BenDavid O, Izraeli ES, Hauri E, Navon O (2007) Fluid inclusions in diamonds from the Diavik mine, Canada and the evolution of diamond-forming fluids. Geochim Cosmochim Ac 71:723–744

Klein-BenDavid O, Logvinova AM, Schrauder M, Spetius ZV, Weiss Y, Hauri EH, Kaminsky FV, Sobolev NV, Navon O (2009) High-Mg carbonatitic microinclusions in some Yakutian diamonds—a new type of diamond-forming fluid. Lithos 112:648–659

Klein-BenDavid O, Pearson DG, Nowell GM, Ottley C, McNeill JCR, Cartigny P (2010) Mixed fluid sources involved in diamond growth constrained by Sr–Nd–Pb–C–N isotopes and trace elements. Earth Planet Sc Lett 289:123–133

Kurz MD, Gurney JJ, Jenkins WJ, Lott DE (1987) Helium isotopic variability within single diamonds from the Orapa kimberlite pipe. Earth Planet Sc Lett 86:57–68

Lee JY, Marti K, Severinghaus JP, Kawamura K, Yoo HS, Lee JB, Kim JS (2006) A redetermination of the isotopic abundances of atmospheric Ar. Geochim Cosmochim Ac 70:4507–4512

Mendelssohn M, Milledge H (1995) Geologically significant information from routine analysis of the mid-infrared spectra of diamonds. Int Geol Rev 37:95–110

Mohapatra RK, Honda M (2006) "Recycled" volatiles in mantle-derived diamonds—Evidence from nitrogen and noble gas isotopic data. Earth Planet Sc Lett 252:215–219

Moreira M, Kunz J, Allègre C (1998) Rare gas systematics in popping rock: isotopic and elemental compositions in the upper mantle. Science 279:1178–1181

Navon O (1999) Diamond formation in the Earth's mantle. In: Gurney JJ, Gurney JL, Pascoe MD, Richardson SH (eds) The J.B. Dawson Volume, Proceedings of the VIIth International Kimberlite Conference. Red Roof Design, Capetown, pp 584–604

Navon O, Hutcheon I, Rossman G, Wasserburg G (1988) Mantle-derived fluids in diamond micro-inclusions. Nature 335:784–789

Ozima M, Zashu S (1991) Noble gas state of the ancient mantle as deduced from noble gases in coated diamonds. Earth Planet Sc Lett 105:13–27

Parman SW, Kurz MD, Hart SR, Grove TL (2005) Helium solubility in olivine and implications for high 3 He/4 He in ocean island basalts. Nature 437:1140–1143

Phillips D, Harris JW, Viljoen KS (2004) Mineral chemistry and thermobarometry of inclusions from De Beers Pool diamonds, Kimberley, South Africa. Lithos 77:155–179

Rapp RP, Timmerman S, Lowczak J, Jaques AL (2017) Metasomatism of cratonic lithosphere by hydrous, silica-rich fluids derived from recycled sediment: experimental insights at 5-7 GPa. Extended abstracts, the Eleventh Int Kimberlite conference, 4640, pp 1-3

Rickard RS, Harris JW, Gurney JJ, Cardoso P (1989) Mineral inclusions in diamonds from Koffiefontein Mine. In: Ross J et al (eds) Kimberlites and related rocks: Their mantle/crust setting, diamonds and diamond exploration. Geol Soc Australia Spec Publ 14 vol 2. Blackwells Scientific Press, Oxford, pp 1054–1062

Sasada T, Hiyagon H, Bell K, Ebihara M (1997) Mantle-derived noble gases in carbonatites. Geochim Cosmochim Ac 61:4219–4228

Schrauder M, Koeberl C, Navon O (1996) Trace element analyses of fluid-bearing diamonds from Jwaneng, Botswana. Geochim Cosmochim Ac 60:4711–4724

565 Schrauder M, Navon O (1994) Hydrous and carbonatitic mantle fluids in fibrous diamonds from
566 Jwaneng, Botswana. Geochim Cosmochim Ac 58:761–771

567 Smith CB, Allsop H, Kramers J, Hutchinson G, Roddick J (1985) Emplacement ages of Jurassic-
568 Cretaceous South African kimberlites by the Rb-Sr method on phlogopite and whole-rock samples.
569 Trans Geol Soc S Afr 88:249–266

570 Stachel T, Harris J (2008) The origin of cratonic diamonds—constraints from mineral inclusions. Ore
571 Geol Rev 34:5–32

572 Staudacher T, Allègre CJ (1982) Terrestrial xenology. Earth Planet Sc Lett 60:389–406

573 Staudacher T, Allègre CJ (1988) Recycling of oceanic crust and sediments: the noble gas subduction
574 barrier. Earth Planet Sc Lett 89:173–183

575 Staudacher T, Sarda P, Richardson SH, Allègre CJ, Sagna I, Dmitriev LV (1989) Noble gases in basalt
576 glasses from a Mid-Atlantic Ridge topographic high at 14°N: geodynamic consequences. Earth Planet
577 Sc Lett 96:119–133

578 Stern RA, Palot M, Howell D, Stachel T, Pearson DG, Cartigny P, Oh A (2014) Methods and reference
579 materials for SIMS diamond C-and N-isotope analysis. Canadian Centre for Isotopic Microanalysis,
580 Research Report 14-01. University of Alberta, Education and Research Archive.

581 Stroncik NA, Haase KM (2004) Chlorine in oceanic intraplate basalts: Constraints on mantle sources
582 and recycling processes. Geology 32:945–948

583 Sumino H, Kaneoka I, Matsufuji K, Sobolev AV (2006) Deep mantle origin of kimberlite magmas
584 revealed by neon isotopes. Geophys Res Lett 33:L16318

585 Timmerman S, Jaques AL, Weiss Y, Harris JW (2018) N-δ13C-inclusion profiles of cloudy diamonds
586 from Koffiefontein: Evidence for formation by continuous Rayleigh fractionation and multiple fluids.
587 Chem Geol 483:31–46

588 Tolstikhin I, Kamenskii I, Sharkov I (1985) Isotopes of Light Inert Gases in Carbonates from the Kola
589 Peninsula. Center Russian Acad Sci, Apatity

590 Tomlinson E, Jones A, Harris J (2006) Co-existing fluid and silicate inclusions in mantle diamond. Earth
591 Planet Sc Lett 250:581–595

592 Turner G, Burgess R, Bannon M (1990) Volatile-rich mantle fluids inferred from inclusions in diamond
593 and mantle xenoliths. Nature 344:653–655

594 Veksler IV, Dorfman AM, Dulski P, Kamenetsky VS, Danyushevsky LV, Jeffries T, Dingwell DB
595 (2012) Partitioning of elements between silicate melt and immiscible fluoride, chloride, carbonate,

phosphate and sulfate melts, with implications to the origin of natrocarbonatite. Geochim Cosmochim Ac 79:20–40

Wada N, Matsuda JI (1998) A noble gas study of cubic diamonds from Zaire: constraints on their mantle source. Geochim Cosmochim Ac 62:2335–2345

Weiss Y, Kiflawi I, Navon O (2010) IR spectroscopy: quantitative determination of the mineralogy and bulk composition of fluid microinclusions in diamonds. Chem Geol 275:26–34

Weiss Y, Griffin W, Navon O (2013) Diamond-forming fluids in fibrous diamonds: the trace-element perspective. Earth Planet Sc Lett 376:110–125

Weiss Y, Kiflawi I, Davies N, Navon O (2014) High-density fluids and the growth of monocrystalline diamonds. Geochim Cosmochim Ac 141:145–159

Weiss Y, McNeill J, Pearson DG, Nowell GM, Ottley CJ (2015) Highly saline fluids from a subducting slab as the source for fluid-rich diamonds. Nature 524:339–342

Weiss Y, Navon O, Goldstein SL, Harris JW (2018) Inclusions in diamonds constrain thermo-chemical conditions during Mesozoic metasomatism of the Kaapvaal cratonic mantle. Earth Planet Sc Lett 491:134–147

Wilding MC (1990) A study of diamonds with syngenetic inclusions. Unpublished PhD Thesis, Uni Edinburgh, 281 pp

Zedgenizov DA, Harte B, Shatsky VS, Politov AA, Rylov GM, Sobolev NV (2006) Directional chemical variations in diamonds showing octahedral following cuboid growth. Contrib Mineral Petrol 151:45–57

Zedgenizov DA, Ragozin AL, Shatsky VS, Araujo D, Griffin WL, Kagi H (2009) Mg and Fe-rich carbonate–silicate high-density fluids in cuboid diamonds from the Internationalnaya kimberlite pipe (Yakutia). Lithos 112:638–647

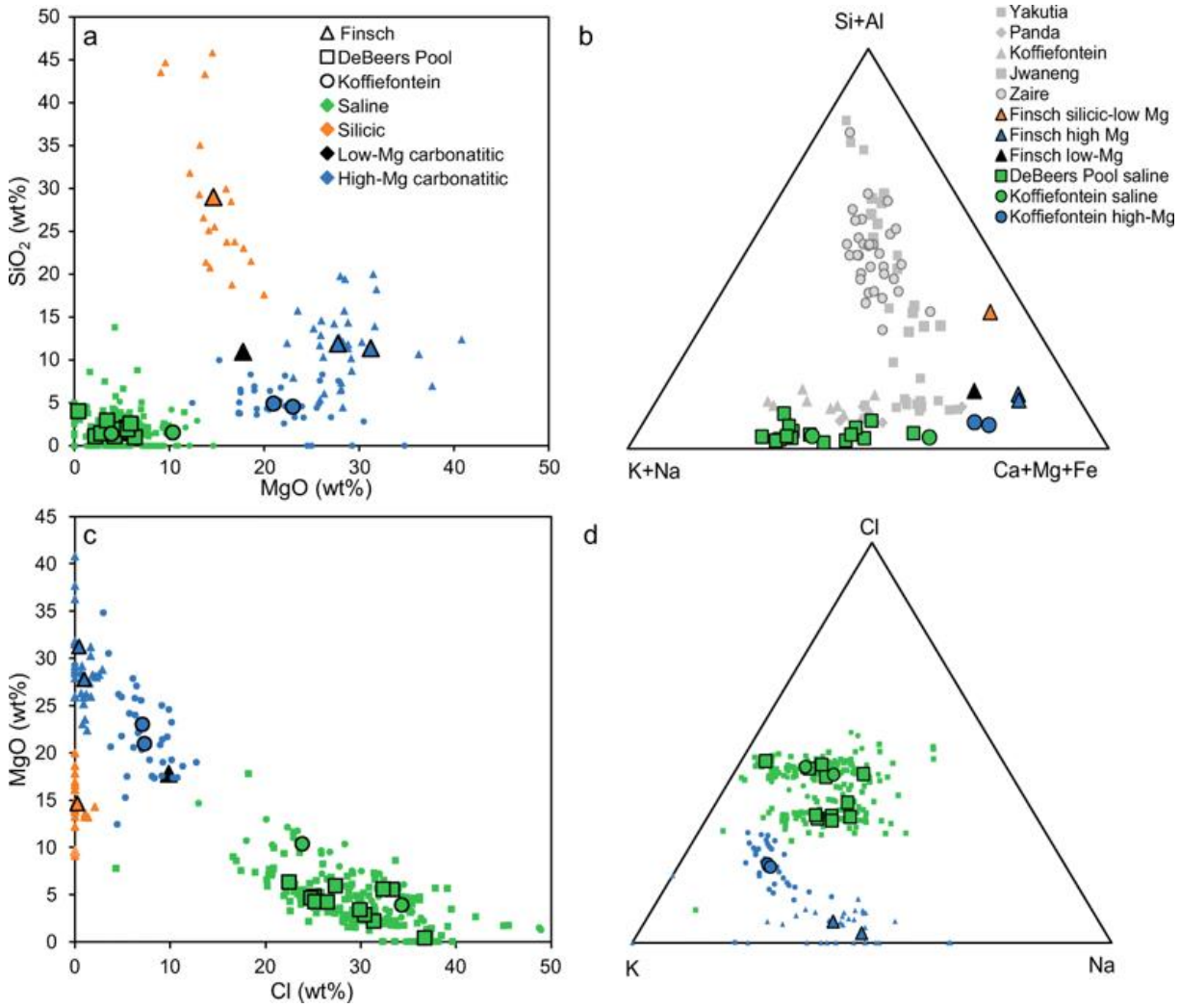

Fig. 1

a SiO_2 versus MgO diagram, distinguishing saline, silicic to low-Mg carbonatitic, and high-Mg carbonatitic HDF compositions. Small symbols are for individual analyses, large symbols for the average of each growth zone. b Triangular Si + Al, K + Na, Ca + Mg + Fe diagram showing the range in major element compositions (in mol%) of the different HDF end-members. The studied samples cover the saline to high-Mg carbonatitic compositional range and part of the low-Mg carbonatitic to silicic range. The compositions of HDF inclusions in diamonds from Yakutia (Zedgenizov et al. 2009), Panda (Tomlinson et al. 2006), Koffiefontein (Izraeli et al. 2001, 2004), Jwaneng (Schrauder and Navon 1994), and Zaire (Navon et al. 1988; Schrauder and Navon 1994) are shown for comparison. c MgO versus Cl diagram showing the range from saline to high-Mg carbonatitic HDF compositions. d Triangular Cl-Na-K diagram showing the decrease in Cl from saline to high-Mg carbonatitic HDF compositions in the studied samples

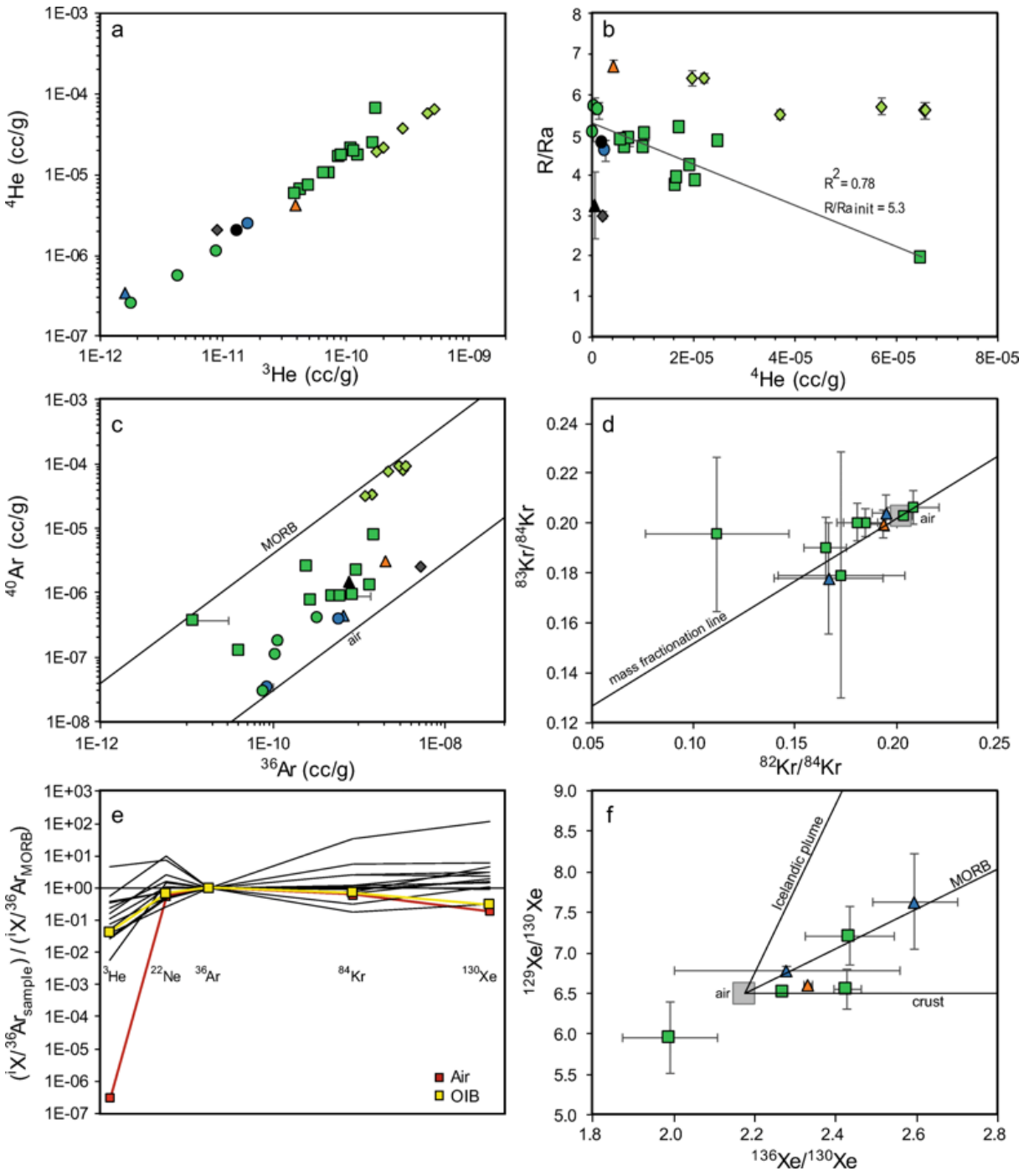

633

634 Fig. 2

635 Noble gas concentrations in the studied diamonds, with fully propagated 1SD errors based on the
636 analytical error, uncertainty in mass discrimination, and uncertainty in the blank. Small diamond
637 symbols in pale green and grey are literature data from Burgess et al. (2009); in their study different
638 HDF compositions were distinguished based on Cl-Ca-K analyses of irradiated samples and not by
639 EPMA analyses of individual inclusions. a Range in helium concentrations: saline inclusions generally
640 have higher ^{3}He and ^{4}He concentrations than silicic and carbonatitic inclusions in diamonds. b Helium
641 isotope compositions (R/Ra = ^{3}He/^{4}He$_{sample}$/^{3}He/^{4}He$_{air}$) versus ^{4}He concentration. Saline diamonds have

642 higher ^{4}He concentrations. Silicic and carbonatitic diamonds show a large range in R/Ra for their
643 relatively low ^{4}He concentrations. c Overlap in Ar concentrations of the various HDF end-members. c
644 For comparison the MORB (40,000) and air (298.6) ^{40}Ar/^{36}Ar ratios are given over the range of
645 concentrations. d Krypton isotope compositions with 2SD. The air composition and mass fractionation
646 line are also shown. e Noble gas abundance patterns. Each stable isotope is normalised to the abundance
647 of ^{36}Ar, and subsequently expressed relative to the MORB abundance ratio (Moreira et al. 1998). f)
648 Xenon isotope compositions (+1SD) with mixing lines of air with MORB, OIB (Iceland plume), and
649 crust (Staudacher and Allègre 1982). One sample is lower than the atmospheric composition, but within
650 2SD uncertainty

651

652

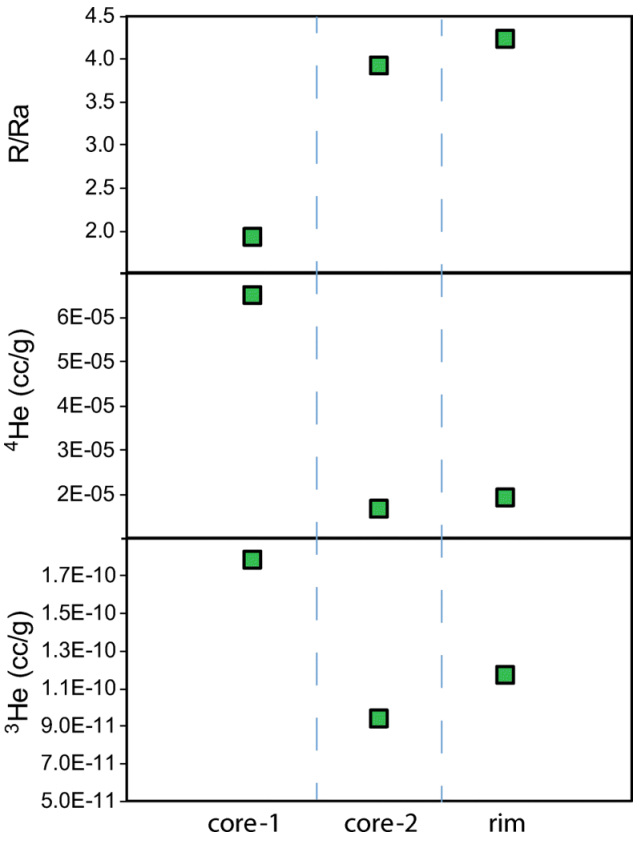

653

654 Fig. 3

655 Differences in He isotopic composition and concentrations between the core, intermediate and rim
656 growth zones of fibrous diamond DBP15. The errors (1SD) are smaller than symbol size

657

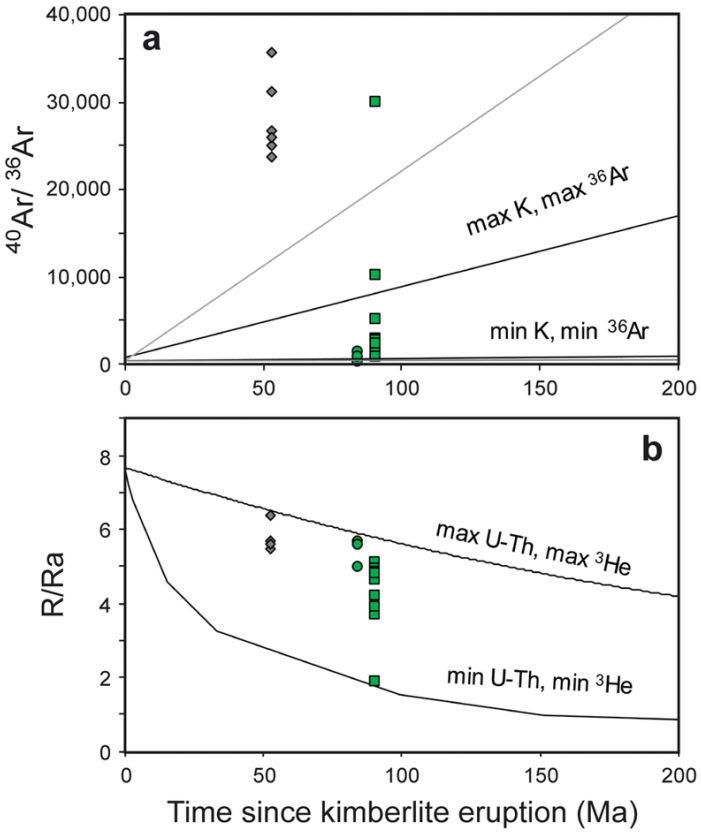

658

659 Fig. 4

660 Change in $^{40}Ar/^{36}Ar$ ratios (a) and R/Ra values (b) over time since kimberlite eruption (symbols of each
661 mine are present-day; for example, 84 Ma has elapsed for Koffiefontein samples since kimberlite
662 eruption). Black model lines were calculated with the minimum and maximum U-Th-K concentrations
663 reported by Weiss et al. (2013) for saline diamonds and the minimum and maximum ^{3}He and ^{36}Ar
664 contents of the present study. a Grey model lines were calculated with the minimum ingrowth based on
665 K and 36Ar data of diamond KOF17b and maximum ingrowth based on K and ^{36}Ar data of diamond
666 DBP15b, assuming a 60–40 wt% oxide to volatile fraction for the K calculation. For argon the following
667 equation was used: $(^{40}Ar/^{36}Ar)t = (^{40}Ar/^{36}Ar)init + (0.109 \times 0.000117 \times K \times (e^{\lambda t}-1))/^{36}Ar$, where 0.109
668 represents the factor for the decay to ^{40}Ar (0.891 decays to ^{40}Ca) and 0.0117% of K is ^{40}K. For the initial
669 $^{40}Ar/^{36}Ar$ the minimum value of 381 observed in the present study is used. b For the helium isotope
670 composition the following formula was used: $(^{4}He/^{3}He)t = (^{4}He/^{3}He)init + (8 \times {}^{238}U \times (e^{\lambda t}-1) + 7 \times$
671 $(^{238}U/137.88) \times (e^{\lambda t}-1) + 6 \times {}^{232}Th \times (e^{\lambda t}-1))/^{3}He$. An initial R/Ra value of 7.7 was assumed. Grey
672 diamond symbols represent saline diamonds from Panda (Burgess et al. 2009), green square symbols
673 the saline diamonds from DeBeers Pool and Koffiefontein (this study)

674

675

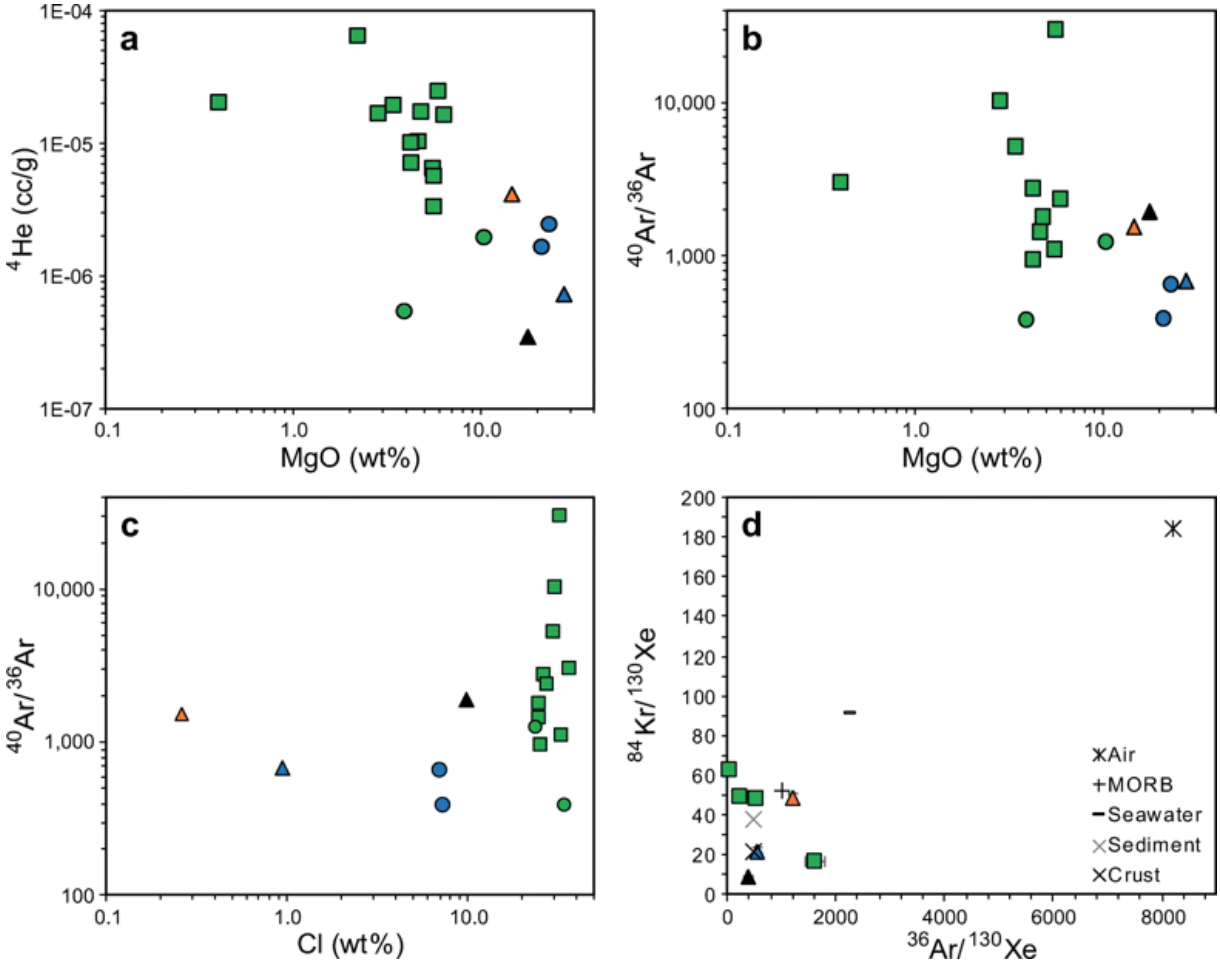

676

677 Fig. 5

678 a ^{4}He versus MgO concentrations showing the dependence of ^{4}He on HDF composition. b, c ^{40}Ar/^{36}Ar
679 ratios versus MgO and Cl contents. Results from KOF19 were excluded from this graph as its major
680 element composition represents a mixture of saline HDF/halides + (K,Na) carbonates instead of a pure
681 HDF composition. d ^{36}Ar/^{130}Xe ratio versus ^{84}Kr/^{130}Xe ratio to distinguish between mantle, air and
682 recycled components, with literature values of these end-members from Mohapatra and Honda (2006
683 and references therein). The plotted Ar/Xe and Kr/Xe ratios are upper limits for sediments and crust, as
684 their values are not well known and lighter noble gases are lost relative to heavier noble gases during
685 subduction

686

Table 1

Average major element composition of fluid inclusions and carbon isotope composition and nitrogen concentration of the diamond host

Sample	Comment	Mine	Fluid %*	sd	$\delta^{13}C_{VPDB}$ (‰)	N (at.ppm)	n=***	Type	Na_2O (wt%)	MgO (wt%)	Al_2O_3 (wt%)	SiO_2 (wt%)	P_2O_5 (wt%)	Cl (wt%)	K_2O (wt%)	CaO (wt%)	TiO_2 (wt%)	FeO (wt%)	Total (wt%)
FIN1a	polycrystalline	Finsch	16.25	4.07	-6.29	640	8	high-Mg	8.08	31.24	2.79	11.38	1.49	0.41	8.83	25.03	0.52	10.23	5.93
FIN1b	core-int	Finsch	0.14	0.01	-6.20	750	25	high-Mg	6.98	27.77	2.28	11.91	3.24	0.95	9.87	21.79	1.42	13.79	7.05
FIN02	whole stone	Finsch	0.13	0.11	-5.09	-**	21	silicic	1.37	14.65	4.48	28.98	2.42	0.26	8.88	15.74	4.03	19.20	14.19
FIN03	whole stone	Finsch	<0.01	-	-3.39	<30	1	low-Mg	13.95	17.76	3.97	10.94	0.00	9.84	8.71	16.87	0.00	17.96	6.95
DBP06	whole stone	DeBeers Pool	3.37	0.37	-6.69	-	19	saline	21.48	5.52	0.76	2.14	0.56	33.33	24.28	5.29	0.00	6.63	9.08
DBP07	core	DeBeers Pool	1.84	0.31	-4.41	330	17	saline	4.13	0.40	0.19	4.04	0.24	36.73	40.08	3.44	0.00	10.75	13.06
DBP08a	polycrystalline	DeBeers Pool	8.56	0.44	-7.08	-	12	saline	23.78	4.79	0.08	1.44	0.39	25.13	31.09	6.01	0.00	7.29	10.87
DBP08b	int	DeBeers Pool	8.2	0.21	-7.63	-	11	saline	20.14	4.63	0.13	1.65	0.31	24.79	33.35	6.68	0.13	8.20	13.66
DBP09a	core	DeBeers Pool	0.61	0.27	-6.56	-	10	saline	19.46	6.33	0.00	1.00	0.00	22.48	31.83	9.71	0.00	9.18	8.66
DBP09b	int	DeBeers Pool	4.79	0.59	-6.44	-	12	saline	18.76	4.24	0.17	1.11	0.00	25.18	37.27	6.85	0.00	6.42	12.58
DBP09c	rim	DeBeers Pool	11.84	1.13	-6.59	-	18	saline	18.49	4.23	0.07	1.92	0.07	26.49	38.12	5.31	0.00	5.31	12.42
DBP10a	core	DeBeers Pool	0.26	0.09	-5.08	470	10	saline	15.38	5.59	0.16	1.93	0.64	32.39	30.50	6.96	0.00	6.45	14.62
DBP10b	int-rim	DeBeers Pool	0.48	0.37	-8.05	520	10	saline	15.38	5.59	0.16	1.93	0.64	32.39	30.50	6.96	0.00	6.45	14.62
DBP14	whole stone	DeBeers Pool	10.06	0.57	-6.94	-	13	saline	21.34	5.91	0.23	2.58	0.75	27.36	29.36	4.85	0.74	6.90	11.08
DBP15a	core-1	DeBeers Pool	3.47	0.90	-5.9	-	14	saline	10.32	2.20	0.00	1.12	0.44	31.38	30.03	7.14	0.00	17.36	11.55
DBP15b	core-2	DeBeers Pool	10.67	1.05	-6.3	-	11	saline	11.83	2.83	0.00	1.46	0.00	30.43	26.15	5.89	0.20	21.21	11.19
DBP15c	rim	DeBeers Pool	14.24	1.28	-5.92	-	30	saline	10.38	3.41	0.25	2.94	0.07	29.91	28.43	5.59	0.10	18.92	12.64
KOF17a	core	Koffiefontein	0.07	0.04	-4.94	800	20	high-Mg	6.61	23.01	1.71	4.55	0.57	7.07	22.30	25.12	0.62	8.45	9.15
KOF17b	rim	Koffiefontein	0.01	-	-4.89	500	18	high-Mg	7.45	20.97	1.70	4.93	0.34	7.30	23.77	20.77	0.92	11.84	9.17
KOF18a	light CL	Koffiefontein	0.07	0.06	-5.42	>510	14	saline	11.93	10.35	0.74	1.55	0.90	23.88	21.04	14.69	0.00	14.91	5.37
KOF18b	dark CL	Koffiefontein	0.07	0.06	-5.45	>450	16	saline	11.03	3.90	0.53	1.41	0.41	34.33	32.72	7.28	0.00	8.39	5.21
KOF19a	core	Koffiefontein	<0.01	-	-6.41	>620	****	saline											
KOF19b	int-rim	Koffiefontein	<0.01	-	-6.37	>540		saline											

[a]Volume fraction of samples that consists of fluid inclusions (determined by counting statistics on BSE images)

[b]n.d. = not determined (due to too noisy FTIR spectra, no estimation of concentrations was possible)

[c]n = number of individual fluid inclusion analyses that were used to calculate the average. Note that no results are reported for KOF19. Means for 13 inclusions in this sample, which likely represents a mixture of halide and (Na,K)-carbonate instead of a fluid composition, are given in Table S1 (Electronic Supplementary Material 2)

[d]Total = analytical total as analysed (i.e., before normalisation to 100 wt%). Note that these original totals are extremely low due to HDF inclusions being below the diamond surface and the presence of volatiles (e.g. H_2O, CO_2) in the inclusions. Results of individual analyses for major elements, $\delta^{13}C$ and N can be found in Table S2, S3, and S4 (Electronic Supplementary Material 2)

Table 2

Noble gas isotope compositions and abundances of fibrous diamond growth zones

Sample	Weight (mg)	^{4}He (cc/g)	sd	^{3}He (cc/g)	sd	R/Ra	sd	^{20}Ne (cc/g)	sd	^{40}Ar (cc/g)	sd	^{40}Ar/^{36}Ar	sd	^{84}Kr (cc/g)	sd	^{132}Xe (cc/g)	sd
FIN01b	29.1	7.31E-07	6.20E-09	na	-	na	-	-*	-	4.52E-07	1.79E-08	682	14	2.67E-11	8.91E-13	9.08E-12	3.29E-13
FIN02	79.8	4.14E-06	3.42E-08	3.93E-11	8.52E-13	6.69	0.15	8.05E-10	9.02E-12	3.12E-06	1.19E-07	1543	15	8.26E-11	2.15E-12	1.14E-11	2.13E-13
FIN03	47.6	3.49E-07	3.07E-09	1.61E-12	4.05E-13	3.25	0.82	-	-	1.50E-06	5.71E-08	1942	51	1.86E-11	6.14E-13	1.44E-11	1.05E-13
DBP06	49.8	6.51E-06	5.37E-08	4.33E-11	9.35E-13	4.68	0.1	4.09E-10	2.91E-11	9.34E-07	3.55E-08	1104	20	-	-	-	-
DBP07	36.4	2.05E-05	1.70E-07	1.12E-10	2.40E-12	3.85	0.08	8.33E-10	3.05E-11	1.25E-07	4.77E-09	3032	274	5.62E-11	1.19E-12	6.52E-12	1.46E-13
DBP08a	37.8	1.74E-05	1.43E-07	1.27E-10	2.68E-12	5.15	0.11	3.52E-10	3.86E-11	8.91E-07	3.40E-08	1801	98	4.36E-11	1.05E-12	6.12E-12	1.58E-13
DBP08b	17.7	1.04E-05	8.54E-08	7.38E-11	2.18E-12	4.99	0.15	1.22E-09	6.95E-11	9.00E-07	3.59E-08	1436	1667	-	-	-	-
DBP09a	7.6	1.66E-05	1.36E-07	8.81E-11	3.08E-12	3.75	0.13	-	-	-	-	-	-	-	-	-	-
DBP09b	21.5	7.17E-06	5.92E-08	4.98E-11	1.81E-12	4.89	0.18	9.83E-10	2.61E-11	1.31E-06	5.16E-08	950	22	-	-	-	-
DBP09c	29.9	1.02E-05	8.39E-08	6.74E-11	1.73E-12	4.67	0.12	3.37E-10	1.05E-10	7.67E-07	3.03E-08	2765	326	5.01E-11	1.27E-12	6.24E-12	1.42E-13
DBP10a	12.6	3.36E-06	3.05E-08	na	-	na	-	-	-	-	-	-	-	-	-	-	-
DBP10b	30.4	5.70E-06	4.69E-08	3.94E-11	1.10E-12	4.87	0.14	1.83E-10	1.36E-10	3.65E-07	1.43E-08	30178	45890	1.32E-11	2.57E-13	-	-
DBP14	73.1	2.49E-05	2.05E-07	1.71E-10	3.62E-12	4.83	0.1	-	-	2.23E-06	8.50E-08	2358	91	3.27E-11	6.45E-13	-	-
DBP15a	31.3	6.51E-05	5.37E-07	1.79E-10	3.94E-12	1.94	0.04	-	-	-	-	-	-	-	-	-	-
DBP15b	25.4	1.69E-05	1.39E-07	9.42E-11	2.15E-12	3.93	0.09	2.00E-09	4.36E-11	2.55E-06	9.70E-08	10363	1496	2.82E-10	1.39E-11	1.11E-10	1.08E-12
DBP15c	19.8	1.95E-05	1.60E-07	1.18E-10	2.71E-12	4.24	0.1	9.10E-10	3.20E-11	7.82E-06	2.97E-07	5185	517	1.50E-11	4.45E-13	5.23E-12	2.16E-13
KOF17a	16.1	2.47E-06	2.04E-08	1.61E-11	9.20E-13	4.59	0.26	4.70E-10	5.08E-10	3.85E-07	1.50E-08	652	23	-	-	-	-
KOF17b	34.9	1.67E-06	1.38E-08	na	-	na	-	-	-	3.44E-08	1.77E-09	389	45	7.46E-12	1.74E-13	-	-
KOF18a	59.8	1.97E-06	1.62E-08	1.34E-11	4.93E-13	4.79	0.18	-	-	4.13E-07	1.57E-08	1236	19	7.07E-12	1.45E-13	2.61E-12	5.53E-14
KOF18b	31.4	5.46E-07	4.69E-09	4.41E-12	5.19E-13	5.69	0.67	-	-	2.95E-08	1.12E-09	382	16	-	-	-	-
KOF19a	36.5	1.13E-06	9.33E-09	8.97E-12	4.02E-13	5.61	0.25	-	-	1.77E-07	6.73E-09	1515	83	-	-	-	-
KOF19b	54.1	2.53E-07	2.20E-09	1.81E-12	2.38E-13	5.03	0.66	-	-	1.07E-07	4.06E-09	997	43	3.80E-12	1.03E-13	3.72E-13	2.31E-14

n.a. = not available (as the ^{3}He peak was not automatically detected)

n.d. = not determined (i.e., no data shown for concentrations <2× the blank level)

Kr and Xe isotope compositions are given in Table S5 (Electronic Supplementary Material 2)